Synthesis of ZSM-23 (MTT) zeolites with different crystal morphology and intergrowths: effects on the catalytic performance in the conversion of methanol to hydrocarbons

A. Molino,[a] J. Holzinger,[b] K. A. Łukaszuk,[a] D. Rojo-Gama,[a] A. E. Gunnæs,[c] J. Skibsted,[b] L. F. Lundegaard,[d] S. Svelle,[a*] P. Beato,[d*] S. Bordiga[a,e*] and K. P. Lillerud[a]

[a.]   Center for Materials Science and Nanotechnology, Department of Chemistry, University of Oslo, Oslo, Norway
[b.]   Interdisciplinary Nanoscience Center (iNANO) and Department of Chemistry-, Aarhus University, Denmark
[c.]   Center for Materials Science and Nanotechnology, Department of Physics, University of Oslo, Oslo, Norway
[d.]   Haldor Topsøe A/S, Lyngby, Denmark
[e.]   Department of Chemistry, NIS and INSTM Reference Centre, University of Torino, Via G. Quarello 15, 10135 Torino, Italy

Abstract

A series of zeolite ZSM-23 samples prepared with different organic structure-directing agents, gave rise to crystalline phases, which show a large variety of particle dimensions. A detailed analysis of the structure of these materials revealed the presence of different levels of stacking fault defects when using different recipes. The effect of crystal size and morphology was investigated in the methanol to hydrocarbon reaction at 400 °C, showing a predominant production of hydrocarbons in the range C_3-C_{6+} and negligible amount of aromatics (<3%) in all cases. More importantly, we show that methanol conversion and catalytic lifetime are strongly influenced by small differences in crystal size and morphology due to a preferential crystal growth along the microchannel direction.

1. Introduction

The methanol to hydrocarbon (MTH) reaction is the last step in a process, which is used to upgrade synthesis gas (a mixture of CO/H_2) generated from coal, natural gas or biomass to higher hydrocarbons, through intermediates of methanol, dimethyl ether (DME) or other oxygenates[1]. In the MTH reaction, methanol is converted over solid acid catalysts like aluminosilicates (zeolites) or silicoaluminophosphates (SAPOs), characterized by crystallographically well-defined nano-pores and -cavities (<2 nm).

The MTH reaction has been described as an autocatalytic process[2], in which the propagation steps at steady-state can be described by a dual-cycle hydrocarbon pool mechanism, schematically shown in Scheme 1. In the '*alkene cycle*', small olefins are methylated by methanol or react with other olefins to form higher olefins, which eventually are isomerized and cracked to generate small olefins as products. Alternatively, the higher olefins can be cyclized to form aromatics and alkanes via hydrogen transfer reactions. The aromatics are then acting as the hydrocarbon pool of the '*arene cycle*' in which the main reactions are again methylation and cracking to produce finally a mixture consisting of methylated aromatics, alkanes, and small olefins.
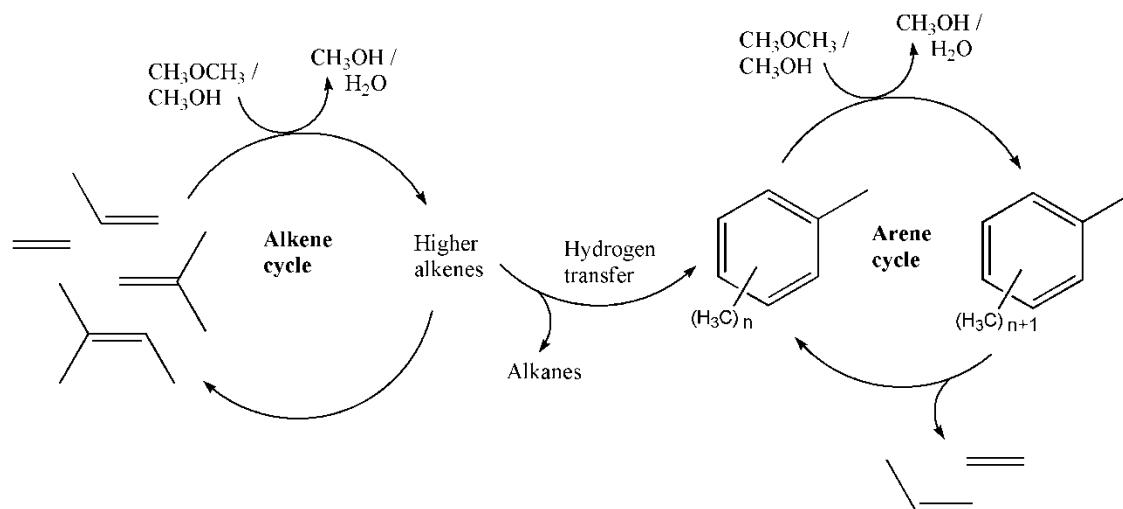
Scheme 1. Simplified scheme of the dual-cycle mechanism. The structures of intermediates and products are dependent on the catalyst used. Adapted from ref [3].

Depending on the specific topology of the employed zeolite (or zeotype) and the applied reaction conditions (temperature, feed rate, pressure) the product selectivity can be tuned and the overall process is named accordingly: methanol to olefins (MTO), methanol to propylene (MTP)[4] or methanol to gasoline (MTG)[5,6].

It has been shown that the ZSM-23 zeolite is highly selective for C_3 to C_6 olefins and produces a low amount of alkanes and aromatics when applied in the MTH reaction[7]. This peculiar behavior has been explained by the concept of shape-selectivity: ZSM-23 is a zeolite of MTT topology with a one-dimensional pore system consisting of channels with an internal diameter of 4.5 x 5.2 Å. Small side pockets are connected to these channels, which generate cavities of 6.2 Å, i.e., similar to the kinetic diameter of a molecule of benzene). The limited pore space effectively suppresses the aromatic-based cycle, which is responsible for the production of aromatics, alkanes, and ethylene, and results in the observed product selectivity. On the other hand, unidirectional microporous materials are inherently prone to diffusion limitations, as discussed by Teketel et al.[8]. To improve the diffusional properties of zeolites, either a secondary mesopore system can be introduced by using templates or post-synthetic treatments like desilication or steaming[9–12], or

nanosized crystals can be prepared[13]. The effect of reducing the crystal size in the MTH reaction has been investigated for several zeolites and zeotypes, like SAPO-34[14,15], SAPO-35[16], ZSM-5[10,15], ZSM-11[17] and ZSM-22[13] and generally, an improvement in catalyst lifetime has been observed whereas the influence on product selectivity is most often less pronounced.[18] We have previously demonstrated that ZSM-23 samples prepared in the presence of different structure-directing agents have very different catalyst lifetimes, which strongly suggests an influence of the crystal size[19]. The scope of this work was to investigate the structural properties of the materials synthesized with different recipes in detail, using a wide range of complementary methods. In addition to the changes in morphology, we also investigated the presence and effect of stacking faults on the MTH reaction. A correlation between pore length and catalyst methanol conversion capacity is proposed while product selectivities remain remarkably constant.

2. Experimental

2.1 Zeolite syntheses

Zeolite ZSM-23 (MTT topology) samples with different morphologies were prepared in-house by hydrothermal synthesis, using synthesis protocols from literature. The batch compositions were adjusted to get similar acid sites concentration. Teflon-lined stainless steel autoclaves were used under tumbling conditions in an oven with a homebuilt rotating inset at 30 rpm for the crystallization. The five samples obtained with different synthesis procedures were labelled according to the used organic structure directing agent (OSDA); PYRR[20] for pyrrolidine, IPA for isopropylamine, HTMPD[21] for a molar mixture of 70% N^1,N^1,N^3,N^3-tetramethylpropane-1,3-

diamine (TMPD) and 30% N^1,N^1,N^3,N^3,2,2-hexamethylpropane-1,3-diamine (HMPD) and

DIQUAT[22–25] as heptamethonium bromide $C_{13}H_{32}Br_2N_2$, DMF[26,27] for N,N-dimethylformamide.

The molar batch compositions of the synthesis gels are reported in Table 1. The details about the

preparation of the catalysts are reported in our previous work.

Table 1. Molar batch compositions.

Catalyst	SiO_2	Al_2O_3	H_2O	Na_2O	SDA	Si source	Al source	SDA type	Time (h)	t (°C)
DMF	1	0.014	29.5	0.36	0.55	Colloidal SiO_2	$Al_2(SO_4)_3$	DMF	94	185
PYRR	1	0.03	45.5	0.20	0.45	Fumed SiO_2	$Al(NO_3)_3$	Pyrrolidine	66	180
IPA	1	0.012	26.7	0.046	2	Fumed SiO_2	$NaAlO_2$	Isopropylamine	92	160
HTMPD	1	0.025	31	0.06	1	Colloidal SiO_2	$NaAlO_2$	30% HMPD/ 70% TMPD	160	160
DIQUAT	1	0.03	40	0.16	0.15	Fumed SiO_2	$Al(NO_3)_3$	Heptamethonium bromide	335	160

2.2 Characterization methods

2.2.1 X-ray diffraction

Powder X-ray diffraction (PXRD) data of the samples (ion-exchanged to H-form; precalcined at

550 °C in air) were collected in the hydrated form in an open capillary in transmission mode (λ =

0.7753 Å) on the Norwegian-Swiss Beamline (BM01) at the European Synchrotron Radiation

Facility (ESRF) in Grenoble (France). The phase identification was performed by Rietveld

refinement using TOPAS-Academic 5 and employing three structure models of the MTT topology

proposed in literature; one with a monoclinic symmetry ($P2_1$)[28] and two with orthorhombic

symmetry (*Pmmn*)[20] and (*Pmn*2_1)[29]. The simulations of powder X-ray diffraction patterns of

stacking fault intergrowths used the DIFFaX module[30] included in the software package GSAS-II (rev. 3246)[31].

2.2.2 Transmission electron microscopy

The size and morphology of the zeolite crystals were determined by transition electron microscopy (TEM). Powdered zeolite samples were crushed in a mortar, dispersed in water and a droplet of the suspension was deposited on a 3 mm lacey carbon film on the copper grid, followed by drying in air. HR-TEM imaging and diffraction was performed on a Jeol JEM-2100F field emission gun microscope operating at 200 kV. Images were acquired with a low-dose approach (Spot Size 1, Alpha 3, down to 0.2 pA/cm^2 on the fluorescent screen) on a Gatan Orius SC200D 2k x 2k pixel CCD camera. The diffraction data were acquired under low-dose conditions to limit the radiation damage, utilizing a more parallel beam (Spot Size 5, Alpha 3).

2.2.3 Fourier transform infrared spectroscopy with CO as probe molecule

Characterization of the acid sites was carried out by Fourier transform infrared spectroscopy (FTIR) using CO as probe molecule. A thin wafer of pure sample powder was supported in a gold envelope inside an in-house-made quartz transmission cell fitted with KBr windows. The sample was pretreated at 150 °C for 1 h and 450 °C for 2 h under vacuum (10^{-6} torr). The sample was cooled to liquid nitrogen temperature and pulses of CO were sent to the cell to increase the CO pressure to reach an equilibrium pressure of around 20 mbar. IR spectra were acquired every pressure increase and decrease step on a Bruker Vertex 80 instrument with an MCT detector in the mid-IR range (4000-450 cm^{-1}) with a resolution of 2 cm^{-1}.

2.2.4 Nuclear magnetic resonance spectroscopy

^{29}Si single-pulse NMR spectra have been acquired on a Varian INOVA-300 spectrometer (7.05 T), using a homebuilt CP/MAS probe for 7 mm o.d. PSZ rotors and a spinning speed of $\nu_R = 7$ kHz. $\pi/4$ excitation pulses ($t_p = 3.0$ ms for $\gamma B_1/2\pi = 40$ kHz, a relaxation delay of 30 s and typically 2048 scans were employed. The $^{29}Si\{^1H\}$ CP/MAS NMR experiments were performed on a Bruker Avance III HD 400 spectrometer (9.4 T), using a homebuilt CP/MAS probe for 7 mm o.d. PSZ rotors. The ^1H spins were initially excited by a ($\pi/2$)-pulse with a field strength of $\gamma B_1/2\pi = 47$ kHz. The contact-time field strengths were $\gamma B_1/2\pi = 41$ kHz (^1H) and $\gamma B_1/2\pi = 27$ kHz (^{29}Si) for contact times of $0.5 - 5$ ms and relaxation delays of 4 s. ^1H decoupling (spinal64) was applied during data acquisition. The ^{29}Si chemical shifts are referenced to neat tetramethylsilane (TMS), using a sample of β-Ca_2SiO_4 ($\delta = -71.33$ ppm) as a secondary reference.

^{27}Al single-pulse NMR spectra have been acquired on a Bruker Advance III 950/54us^2 spectrometer (22.3 T), using a Bruker ^1H-X-Y 2.5 mm MAS probe and a spinning speed of $\nu_R = 30$ kHz. Single pulses with a field strength of 100 kHz and a pulse width of 0.5 μs corresponding to a ($\pi/10$)-pulse were employed. The ^{27}Al chemical shifts are referenced to a 1.0 M aqueous solution of $AlCl_3 \cdot 6H_2O$. For all single-pulse ^{27}Al MAS NMR spectra, a spectrum of an empty rotor recorded under the same experimental conditions has been subtracted since the rotor and probe result in cause a few broad resonances of very low intensity.

2.2.5 N_2 adsorption and BET analysis

The BET surface area and t-plot area were determined by nitrogen physisorption measurements at liquid nitrogen temperature (adsorption-desorption range 0–0.99 p/p_0, BET linearization from 0.05

to 0.15 p/p$_0$) on a Belsorp-mini II instrument. Sample were outgassed under vacuum for 5 h, 1 h at 80 °C, and 4 h at 300 °C prior to the measurement.

2.3 Catalytic tests

The catalytic reactions were performed in a continuous flow U-shaped fix-bed reactor (i.d. of 10 mm). Prior to the reactions, the catalysts were heated from room temperature to 550 °C under a flow of pure O$_2$ and kept for 1 h for an *in-situ* calcination of the catalysts. After the pre-treatment, the reactor was cooled down under a flow of pure He to the temperature applied for the reaction (400 °C).

The methanol to hydrocarbon reaction was carried out at atmospheric pressure and 400 °C. 100 mg of catalyst was used (sieve fraction 250 to 420 μm). A He flow of 19.5 mL min^{-1} was bubbled through a saturator filled with MeOH (BDH Laboratory, purity >99.8 %) at a temperature of 20 °C, giving rise to a methanol partial pressure of 130 mbar. The resulting weight hourly space velocity (WHSV) was 2 g$_{MeOH}$ g$_{catalyst}$$^{-1}$ h^{-1}. The reaction products were analyzed using an online Agilent 6890A gas chromatograph equipped with an SPB-5 capillary column (length 60 m, 0.530 mm i.d., stationary phase thickness of 5 μm) and a flame ionization detector (FID). Methanol conversion (X$_i$) and product selectivity (S$_i$) were obtained by the integration of the areas from the GC-FID chromatogram.

$$S_i(\%) = \frac{area\ of\ HC\ product\ peak\ i}{total\ area\ of\ HC\ product\ peaks} \times 100$$

(eq. 1)

$$X_i(\%) = \frac{area\ of\ HC\ product\ peaks}{total\ corrected\ peak\ area} \times 100$$

(eq. 2)

Both methanol (MeOH) and dimethyl ether (DME) were considered to be reactants and the rest of compounds detected in the GC as products of reaction. Measured response factors were used for MeOH and DME, whereas the response for the hydrocarbons was considered proportional to the number of carbon atoms in the molecule. Selectivities are reported on a carbon basis.

3 Results and discussion

3.1 Zeolite structure and morphology

The powder X-ray diffraction (XRD) data obtained from synchrotron radiation ($\lambda = 0.7753$ Å) are presented in Figure 1. Phase identification was performed by Rietveld refinement, using the three proposed structures for ZSM-23: a structure based on powder XRD and electron diffraction with *Pmmn* symmetry[20]; a structure based on NMR and powder XRD with a monoclinic symmetry ($P2_1$),[28] and the most recent structure based on single-crystal XRD with an orthorhombic symmetry ($Pmn2_1$)[29].
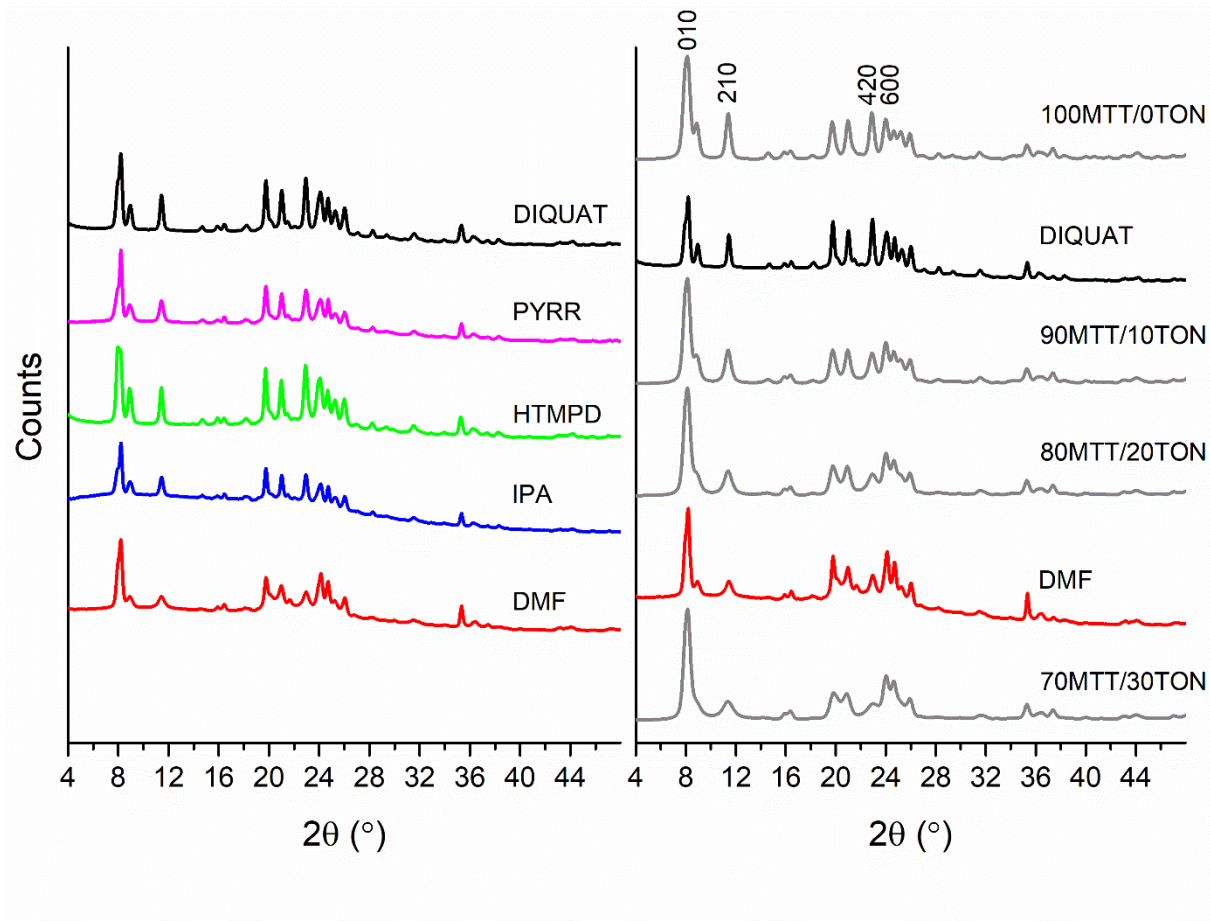
Figure 1. Left: PXRD pattern of different samples of H-ZSM-23. Right: PXRD patterns of the DMF ZSM-23 and DIQUAT ZSM-23 samples compared with the simulated pattern of ZSM-23 (MTT) and ZSM-22 (TON) intergrowths. Scattering angles have been converted for ease of comparison to the Cu Kα lab source (λ = 1.5406 Å).

Compared to the other samples, the diffraction pattern of the DMF sample shows anisotropic peak broadening for all the *hkl* reflections with $k \neq 0$. The most evident peaks are around 2θ values of 11.2 (210) and 22.4 (420),7.8 (010), and 15.6 (020), while for the *h0l* reflections the peak shape is very similar to other samples, with the most evident peak at 2θ = 24.4 (600).

Anisotropic broadenings of XRD patterns are often caused by an anisotropic morphology of crystals in nanometric size. Therefore, the patterns were refined with an ellipsoid model taking into account the average crystallite size along the three crystallographic orientations[32,33] (see

10

Figure S 1-5). Even then, the Rietveld refinement gives a poor fit for the DMF sample (see Figure S 5), indicating that other factors are contributing to the observed anisotropic peak shapes. This is further confirmed by TEM and electron diffraction analysis (*vide infra*, Figure 4) which shows that all samples present a similar dimension along *a* and *b,* from 20 to 50 nm.

However, we have found that the XRD broadening observed for DMF is due to stacking fault defects along the *b* direction. This phenomenon has already been described by Zones et al.[34] for an intergrowth material, MTT/TON, called SSZ-54 (MTT/TON of 70/30), and prepared with a mixture of different templating agents (N-isopropyl-1,3-propanediamine and 1-methylbutylamine). Another intergrowth MTT/TON, called DLZ-02 (MTT/TON of 60/40), has been reported in literature[35], which was prepared by a synthesis involving a dual-template strategy, employing a mixture of Diethylamine (DEA) and Dimethylamine (DMA), which when used alone act as structure-directing agents to prepare zeolites with MTT and TON topologies, respectively[36]. Here, an MTT/TON intergrowth material is made using only a single structure-directing agent (DMF). It is also curious how DMF, probably a DMA precursor, is producing an MTT/TON intergrowth material with a majority of MTT domains, while pure DMA has been used to produce zeolites with TON topology[36]. Such almost opposite structure-directing effect can most probably be explained by the different synthesis conditions in terms of temperature and batch gel composition.

The MTT/TON intergrowths are formed because these structures are made of the same building units (*jbw mtt bik ton*). However, their arrangement in the unit cell generates pores with different symmetry, i.e. mirror plane for the MTT and inversion for TON, generating an AB stacking for MTT (see figure S6 in SI) and ABC for TON (see figure S7 in SI). In order to generate the stacking

sequence, the crystallographic unit cells of MTT and TON need to be decomposed in their A, B and C layers. As evident from Figure 2, when a unit cell of TON is defined (highlighted in blue), some similarities with the MTT structure become apparent. When these cells are cut in half, the A, B and C layer can be obtained (see Figure S 6-7). These layers are not a regular unit-cell, as a shift is needed when repeated in the c-direction.
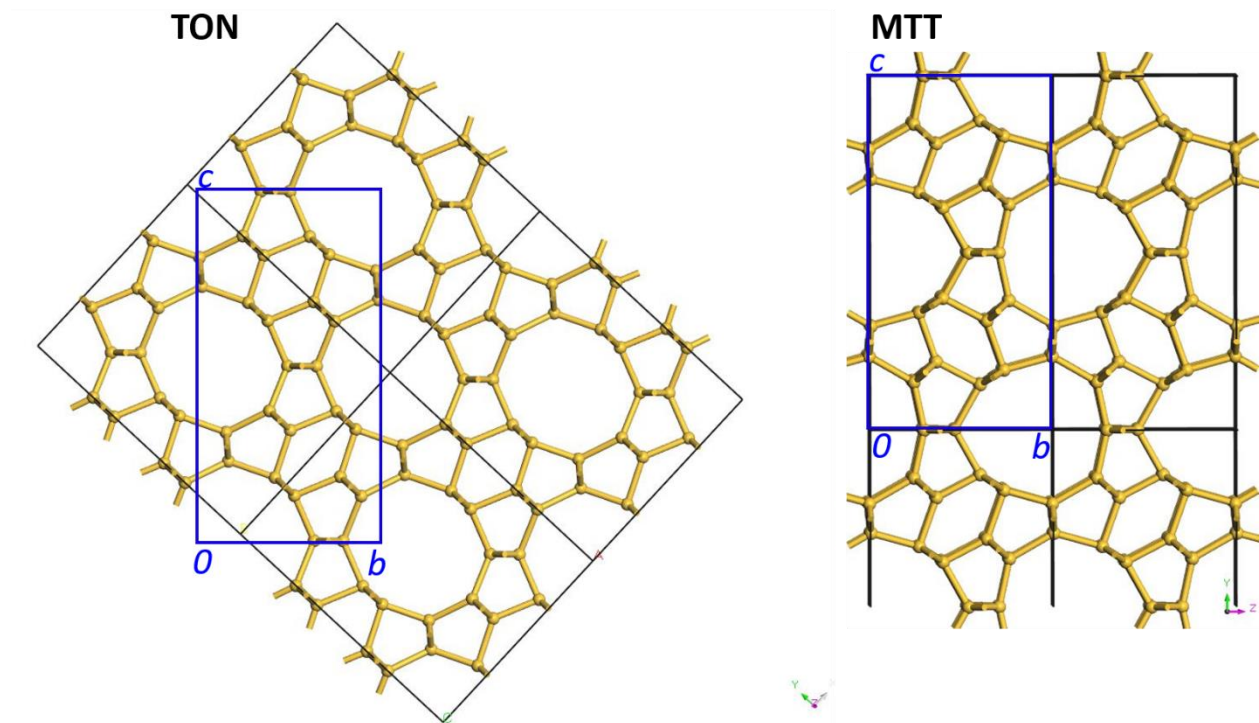

Figure 2. TON (ZSM-22) and MTT (ZSM-23) view along the direction of the 10-ring channels. The crystallographic cells are indicated in grey. For clarity only the T-atoms are represented in the illustrations.

The stacking of MTT in the b-direction is as a sequence alternating two sub-cells, while the stacking of TON along the new b-direction is a sequence of the same sub-cell with a shift of -0.22 in the c-direction. An example of MTT, TON and layer fault is shown in Figure 3.
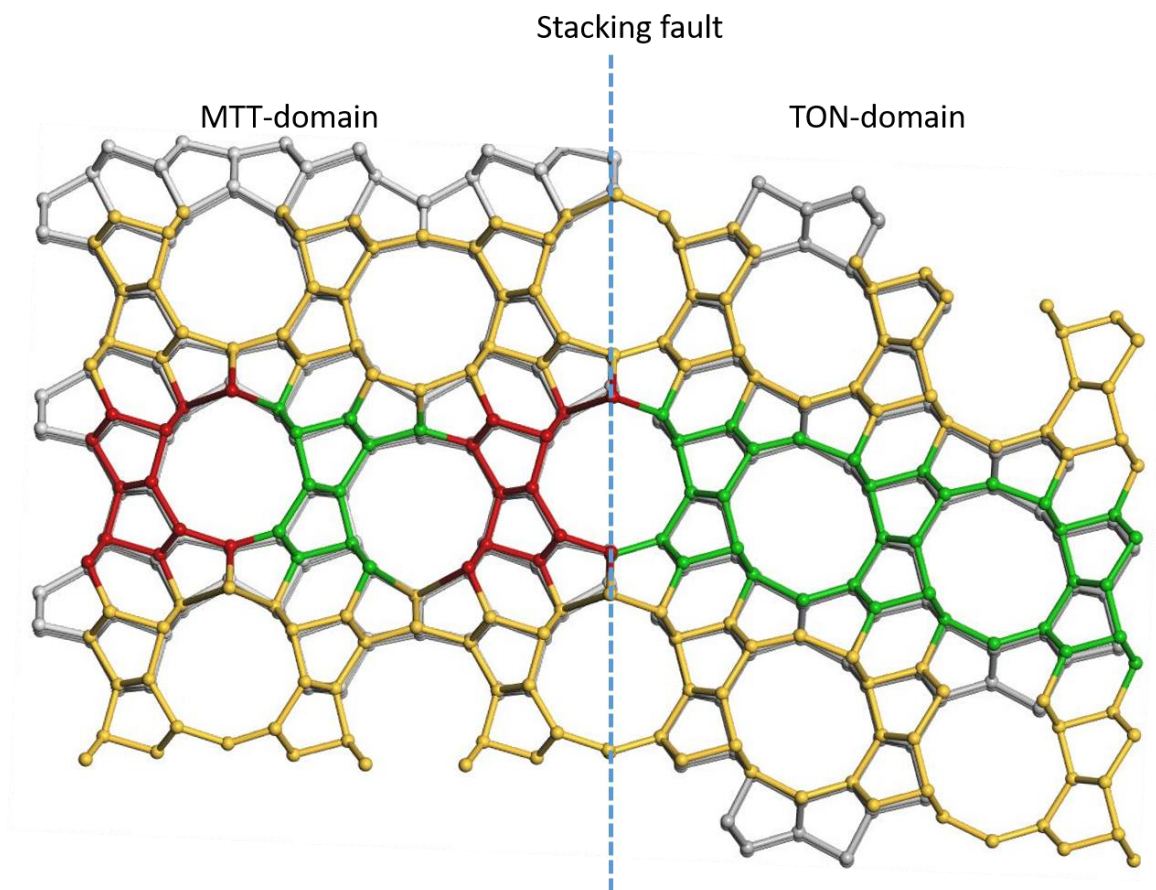
Figure 3. Visualization of a stacking fault at the edge of MTT and TON domains. The channels in the stacking fault are more circular but the change is small compared to the MTT and TON structure.

The faulting is such that it does not block the 1D channels, as the pore size of MTT and TON is the same (10 member) with a small difference in shape. Therefore, the catalytic properties in terms of size and shape selectivity are very similar.

An estimation of the level of stacking faults has been performed by comparing the experimental XRD patterns of our samples with those generated by the simulation of MTT/TON intergrowths at different levels of faulting. In Figure 1, it can be seen how the XRD pattern of the DMF sample is consistent with the simulated pattern of MTT/TON intergrowths with a moderate level of stacking faults (20 - 30% of TON faults). For DIQUAT, the XRD pattern is similar to a stacking fault-free MTT structure (<10% of TON faults) and in a similar way for the other samples (IPA,

PYRR, HTMPD) which for clarity are not included in the graph. The XRD pattern simulation of the full range of stacking fault is reported in Figure S8.

The proposed structure differs from the model of Zones et al.[29] in the absence of atomic disorder, and the presence of water as extra framework species only to remove the contribution of organic template molecules and fluorine. The shortest lattice parameter (c) from the refinement of our data gives a value of 5.05 Å, which is similar to the shortest lattice parameter of the other two models, and thus we assume that the c-axis value of 5.8 Å given by Zones et al.[29] is a typing error. The differences between the models are summarized in Table 2.

Table 2. Proposed MTT model compared with the other models from the literature.

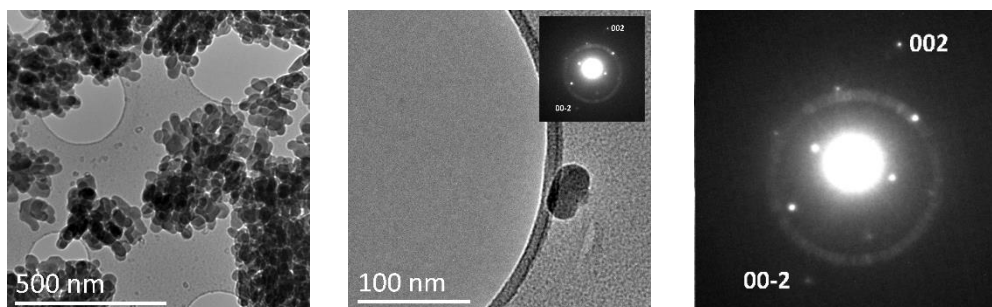| Source	Space group	Lattice parameters				Disordered structure	Extra framework species
		a (A)	b (A)	c (A)	β(°)		
This work	$Pmn2_1$	21.642	11.178	5.052	90	No	H_2O
Rohrman et al. (1985) [20]	$Pmmn$	5.01	21.52	11.13	90	No	None
Mrler et al. (1993) [28]	$P2_1$	11.129	5.025	21.519	89.85	No	NH_4F
Zones et al. (2005) [29]	$Pmn2_1$	21.557	11.170	5.800	90	Yes	HF, Pyrrolidine

* The atomic coordinates are given in Supplementary Information.

The model proposed by Zones et al.[29] was chosen to refine our XRD data, because among the three different models it has the smallest difference in electron density map compared with the simulation of electron density from experimental XRD, as visible in figures S9-11. Because of the nanometric size of the crystallites (equivalent to a tenfold unit cell), the crystal morphology has been further investigated by electron microscopy and diffraction. In addition to the small crystallite size, which makes it impossible to use single crystal X-ray diffraction (SC-XRD), the interaction of X-rays with matter is 10^3 to 10^4 smaller compared to electrons[37–39]. However, care must be taken

since microporous materials are sensitive to the electron beam, especially in case of converged beam conditions used for high resolution imaging. In case of electron diffraction (ED), the optimal conditions are a parallel beam and therefore the dose rate can be reduced by several orders of magnitude.

Figure 4 shows the TEM micrographs and the corresponding selected area electron diffraction (SAED) of all catalysts with MTT topology. All the samples show a rod-like shaped morphology, with a thickness of the rod of 20-30 nm and a length varying from 50 nm to a few microns (see also supplementary information).

The TEM crystal size analyses were performed on a sample size ranging from 60 to 100 crystals of which the results are reported in the histograms in Figure S13, showing an inhomogeneous distribution in crystal sizes, which can be described as a multimodal distribution. However, in the case of the DIQUAT sample, the distribution is unimodal, with crystal length centered on 50 nm and a very narrow distribution. The DMF sample shows crystals with the broadest distribution and length from 50 nm up to 2 μm, with a needle-like morphology (see also additional SEM/TEM images in SI).
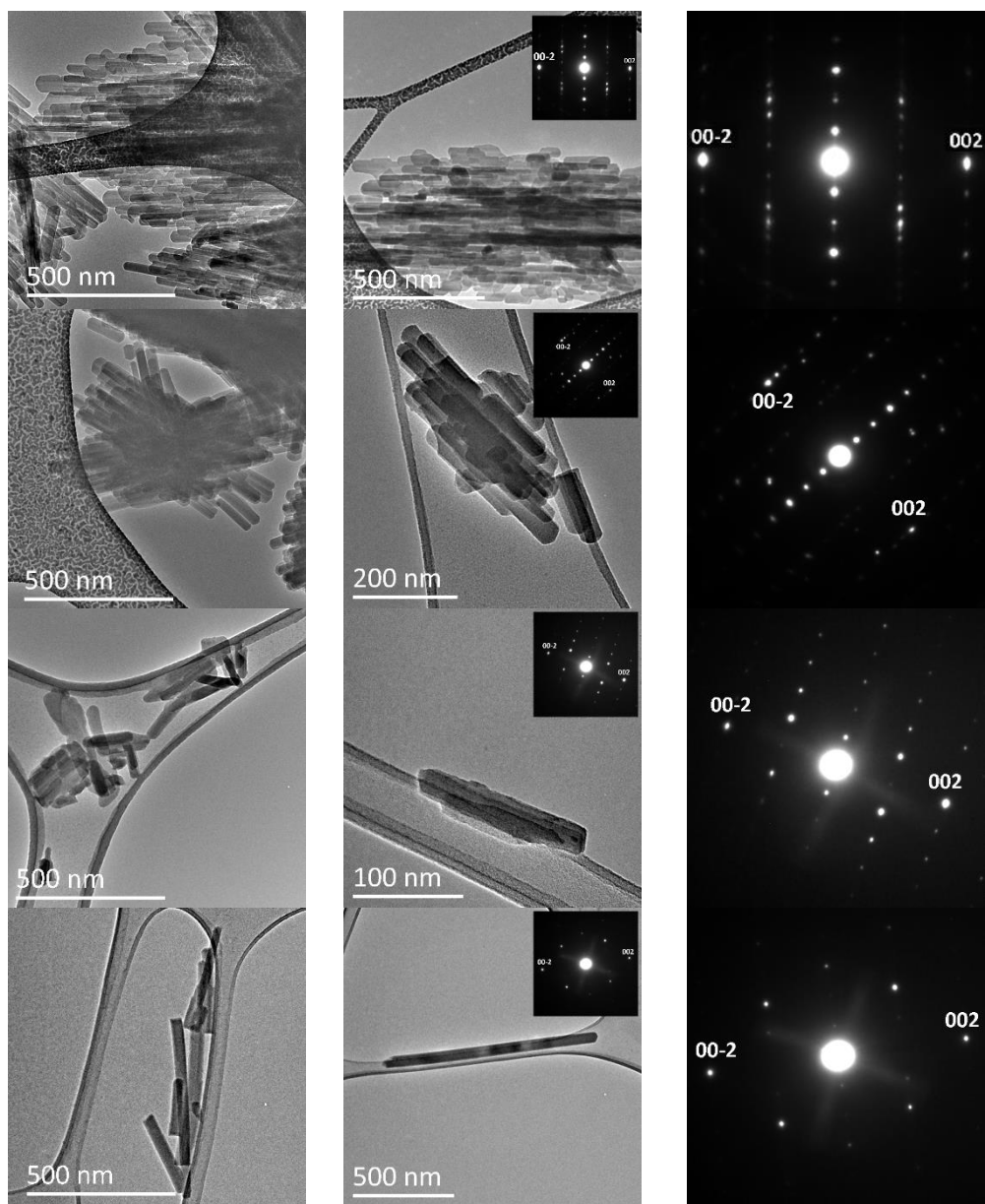
Figure 4. TEM micrographs at two different levels of magnification and SAED patterns (inset) of ZSM-23 samples. From top to bottom DIQUAT, PYRR, HTMPD, IPA, DMF.

The SAED insets in Figure 4 highlight the [00n] diffraction spots arising from the crystals shown in the main figures respectively. From this set of images, it is clear that the observed c-axis (in the SAED images) is parallel to the long axis of the needle-shaped crystallites (TEM images).

3.2 FTIR-CO

Figure 5 shows the FTIR spectra of the samples activated in vacuum at 450 °C before and after adsorption at 100 K of CO at low loading (equilibrium pressure of 0.065 mbar) in absence of physisorbed CO (band at 2140 cm^{-1}). The spectra are normalized by the pellet thickness (integration of the overtone bands around 2000 cm^{-1}). The left panel shows the ν(OH) region, while the right panel shows the ν(CO) region. All samples in the dehydrated form present characteristic bands of Si(OH)Al Brønsted sites at 3610 cm^{-1} and silanol groups at 3745 cm^{-1}, while for the DIQUAT and HTMPD sample also a small band at around 3650 cm^{-1} appears, indicating the presence of a small amount of Al(OH) sites. The needle-like morphology of the DMF sample shows the lowest intensity for the terminal silanols at 3745 cm^{-1}, while for the DIQUAT sample the band is the most intense. This can be explained by the large size difference of the crystals, and consequently the external surface to volume ratio. Upon CO adsorption, the Si(OH)Al band at 3610 cm^{-1} is eroded in favor of a band around 3300 cm^{-1}, while the band around 3745 cm^{-1}, ascribed to silanol groups, is shifted only slightly to generate a weak and broad band at around 3400 cm^{-1}. No significant difference in the magnitude of these shifts can be discerned, indicating a similar/identical acid site strength among the materials, as expected.

For all the samples, the Brønsted band at 3610 cm^{-1} is not completely eroded in presence of CO, suggesting the inaccessibility of some acid sites, presumably due to crystal defects. This phenomenon is more obvious for the DMF sample, which has the highest amount of crystallographic defects combined with the lowest surface area and largest crystal size (see Table 5).

In the CO region, a sharp band of similar intensity around 2175 cm^{-1} appears, indicating a similar acid sites density for all samples. A weak band at 2230 cm^{-1} is present in the spectra of DIQUAT,

17

HTMPD and IPA samples, suggesting the presence of some Al(OH) Lewis sites defects. The FTIR spectra illustrating in detail the CO stretching region are shown in figure S13.
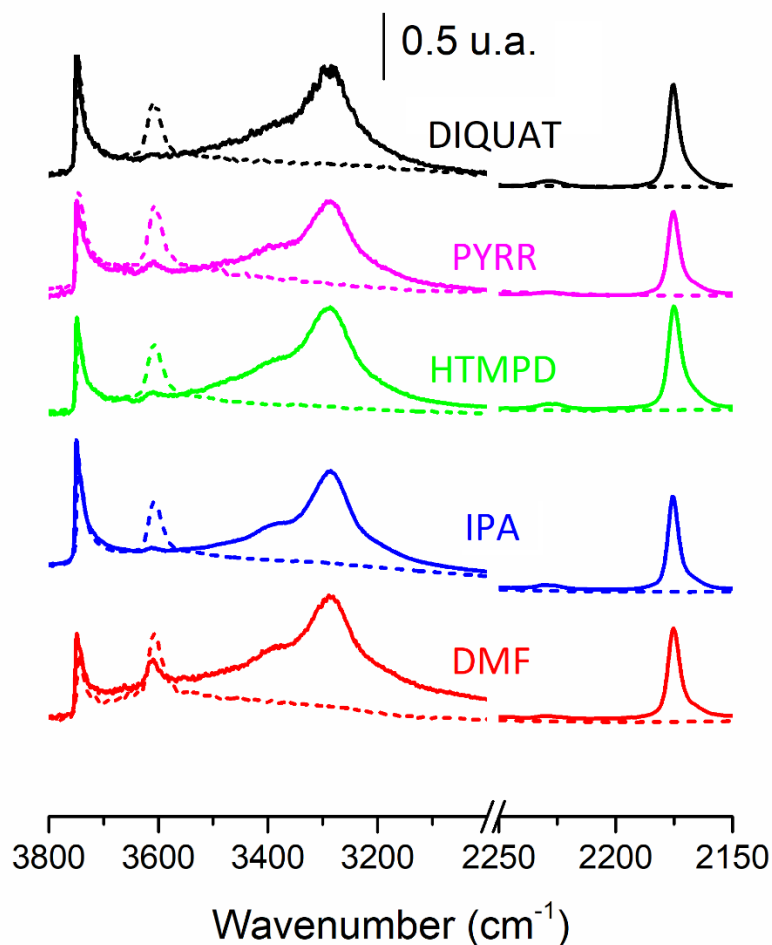

Figure 5. FTIR spectra of ZSM-23 samples activated in vacuum at 450 °C (dashed curves) and after dosing CO at equilibration pressure of 0.065 mbar (solid lines). A linear baseline has been applied and the intensity normalized by the overtone band around 1700-2100 cm^{-1}.

3.3 NMR

The amount of aluminum inside the zeolite framework structure and the types of Si and Al species were investigated by ^{29}Si and ^{27}Al NMR spectroscopy. In the ^{29}Si MAS NMR spectra, shown in

Figure 6, different Si surroundings of the type $Q^m\{n\text{Al}\}$ (*m* being the number of bridging oxygen atoms and *n* the number of connected Al tetrahedra) can be distinguished, as well as Si-OH sites, identified by $^{29}\text{Si}\{^1\text{H}\}$ CP/MAS NMR (Figure S14).
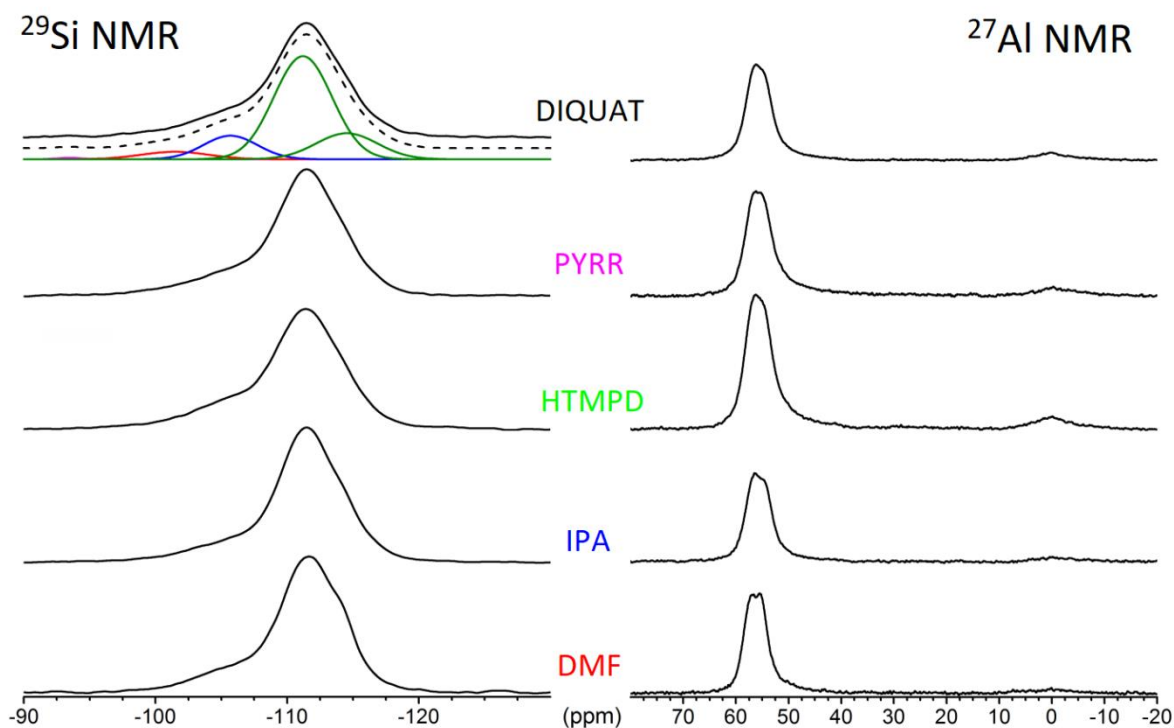

Figure 6. Single-pulse ^{29}Si MAS NMR spectra (left; B_0 = 7.05 T, ν_R =7.0 kHz), including the deconvolution of the spectrum for sample DIQUAT ($Q^2\{0Al\}$ magenta; $Q^3\{0Al\}$ red; $Q^4\{1Al\}$ blue; $Q^4\{0Al\}$ green), and single-pulse ^{27}Al MAS NMR spectra (right; B_0 = 22.3 T, ν_R = 30 kHz) for the H-ZSM-23 samples.

The main resonances in the range of -109 ppm to -116 ppm are assigned to $Q^4\{0\text{Al}\}$ type sites,[40] and they are simulated with two Gaussian-type functions in the deconvolution. Si connected to one Al tetrahedron ($Q^4\{1\text{Al}\}$) are observed at approximately -106 ppm, silanol sites ($Q^3\{0\text{Al}\}$ and $Q^2\{0\text{Al}\}$) at -102 ppm and -94 ppm, respectively. $^{29}\text{Si}\{^1\text{H}\}$ CP/MAS NMR spectra of the DIQUAT sample (Figure S14) prove that the signals at -102 ppm and -94 ppm originate from silanol sites, rather than from a $Q^4\{2\text{Al}\}$ site, utilizing the transfer of magnetization from dipolar-coupled ^1H to ^{29}Si in the CP experiment. These resonances are used in deconvolutions of the ^{29}Si MAS NMR

spectra (Figure 6). The Si/Al ratio of the framework structure can be calculated from the obtained

intensities (I) (Table 3), employing the relationship

$$\frac{\text{Si}}{\text{Al}}(^{29}\text{Si}) = \frac{4\,(I\,[Q^4\{1Al\}+I\,[Q^4\{0Al\}])}{I\,[Q^4\{1Al\}]} \qquad \text{(eq. 3)}$$

This equation holds for highly siliceous zeolites in the absence of direct Al-O-Al bonds

(Loewenstein's rule[41]). In all samples, except sample DIQUAT, the Si/Al ratios from ^{29}Si NMR

are somewhat higher than those determined by EDX.

The fraction of silanol sites ($Q^3\{0Al\}$ and $Q^2\{0Al\}$) ranges from 3% to approx. 6% in the different

samples (Table 3), and they originate from sites at the surface of the crystals and from defect sites

in the framework structure caused among other effects by calcination. In fact, the lowest

concentration of silanol defects detected by NMR (Table 3) for the DMF sample is in agreement

with the lowest surface area (

Table 4) and the lowest intensity of silanol bands around 3740 cm^{-1} in the FTIR spectra (Figure

5).

In the high-field ^{27}Al MAS NMR spectra, acquired at a magnetic field of 22.3 T, central-transition

resonances from four-, five- and six-fold coordinated Al have been identified at chemical shifts of

roughly 55, 25 and 0 ppm, respectively (Figure 6). The high intensity band at 55 ppm is ascribed

to tetrahedral framework sites (T-sites). Al atoms in five- and six-fold coordination are considered

either as extra-framework aluminum (EFAl) from cationic aluminum hydroxide species or

hydroxylated alumina-like species inside the channels, or as a defect-framework aluminum located

in a broken framework structure partly bonded to hydroxyl groups and water caused by, *e.g.*,

calcination. In the samples IPA, HTMPD and PYRR, a minor amount of five-fold coordinated Al

is detected, whereas approx. 10% of six-fold coordinated Al can be found in all samples. Relative intensities for the differently coordinated Al have been determined by simple integration of the ^{27}Al MAS NMR spectra and are summarized in Table 3. These data show that depending on the sample, 7% to 17% of the aluminum has not been incorporated in the framework structure during the synthesis or is present as a defect framework site. Assignment of the five- and six-fold coordinated Al to EFAl allows calculation of a second framework Si/Al ratio from their relative intensities (EFAl%) in combination with the bulk Si/Al ratio from EDX analysis (Table 4), *i.e.* Si/Al ([27]Al) = Si/Al (EDX) / (1- EFAl%). These values are generally in agreement with the framework Si/Al ratios determined from ^{29}Si NMR. Minor deviations probably originate from the simple model used in the simulations of the spectra and the possibility that not all five- and six-fold coordinated Al can be ascribed as EFAl. Some of these sites may be defect sites in the framework structure and thus, they are partly connected to Si framework sites. It appears that ammonia TPD yields systematically higher Si/Al ratios than the other methods (except perhaps for the DIQUAT sample), which might indicate some accessibility issues, in line with FTIR.

Table 3. Summary of the results from ^{27}Al and ^{29}Si NMR.

	^{29}Si NMR[a]				^{27}Al NMR[b]			
Sample	I [Q^2{0Al}]	I [Q^3{0Al}]	I [Q^4{1Al}]	I [Q^4{0Al}]	Al(IV)	Al(V)	Al(VI)	EFAl
DIQUAT	0.4	5.4	13.9	80.4	91.2	0	8.8	8.8
PYRR	0.3	5.8	12.5	81.4	82.9	6.8	10.3	17.1
HTMPD	0	5.8	14.8	79.5	84.6	4.6	10.8	15.4
IPA	0.3	4.5	10.8	84.4	90.3	3.1	6.6	9.7
DMF	0	3.0	12.1	84.9	93.4	0	6.6	6.6

[a] Relative intensities obtained from simulations of the single-pulse ^{29}Si MAS NMR spectra.
[b] Relative intensities from integration of the single-pulse ^{27}Al MAS NMR spectra. The Al(V) and Al(VI) resonances are considered as extra-framework aluminum (EFAl).

Table 4. Comparison of acid concentration and BET surface area (complete adsorption/desorption graph in figure S 15 in SI) of different samples.

Sample	Si/Al molratio (EDX)	Si/Al molratio (NH$_3$-TPD)	Si/Al molratio[a] (^{29}Si NMR)	Si/Al molratio[b] (^{27}Al NMR)	BET Surface Area (m^2/g)	t-plot micropores Surface Area (m^2/g)
DIQUAT	27	31	27	30	276	251
PYRR	23	42	30	28	271	251
HTMPD	18	31	25	21	281	219
IPA	28	47	35	31	264	246
DMF	26	45	32	31	150	134

[a] Si/Al (^{29}Si) ratios of the framework calculated from eq. (3).

[b] Si/Al (^{27}Al) ratios of the framework calculated from the relative intensities of EFAl species from Si/Al (^{27}Al) = Si/Al (EDX) / (100% − EFAl%).

The combination of NMR and FTIR with CO as probe molecule allows a more detailed description of the active sites. In particular, the data obtained from NMR allows a precise quantification the Si/Al ratio of the framework, and the quantification of aluminum in the tetrahedral sites, which is comparable for all the samples, ranging from 83 to 93% of the total amount of aluminum. At the same time, the normalized FTIR spectra suggest a similar Si/Al ratio, due to the similar intensity of the Brønsted site band around 3610 cm^{-1}, but when using CO as probe molecule, some of the Brønsted sites are not interacting with CO, indicating that some acid sites are not accessible. The amounts of silanol sites were also quantified by both techniques giving similar results; the deconvolution of the ^{29}Si NMR spectra estimated their concentration between 3% (DMF sample) and 5.5% (DIQUAT, PYRR, HTMPD), while the FTIR spectra of the activated samples showed the lowest intensity of silanols band for the DMF sample. In contrast, the extra framework aluminum species, which were only seen by FTIR by two weak bands around 3650 cm^{-1} (AlOH stretching) and 2230 cm^{-1} (CO stretching), have been instead quantified precisely by ^{27}Al NMR (Table 3).

3.4 Catalytic test

Figure 7 shows the methanol conversion plotted against the cumulative conversion for a comparison of the performance of the different catalysts. Generally, the shapes of the deactivation curves are similar for all samples, with a rapid deactivation as soon the methanol conversion drops below 80% conversion. It is worth mentioning that the value for the cumulative conversion of the PYRR sample is very similar to the value (11.6 g_{MeOH}/g_{cat}) of the commercial ZSM-23 sample used by Teketel et al.[8] at the same reaction conditions. While the HTMPD, IPA and DMF catalysts show a comparatively lower conversion capacity, the DIQUAT catalyst shows a conversion capacity, which is around an order of magnitude higher compared to the other samples. In order to
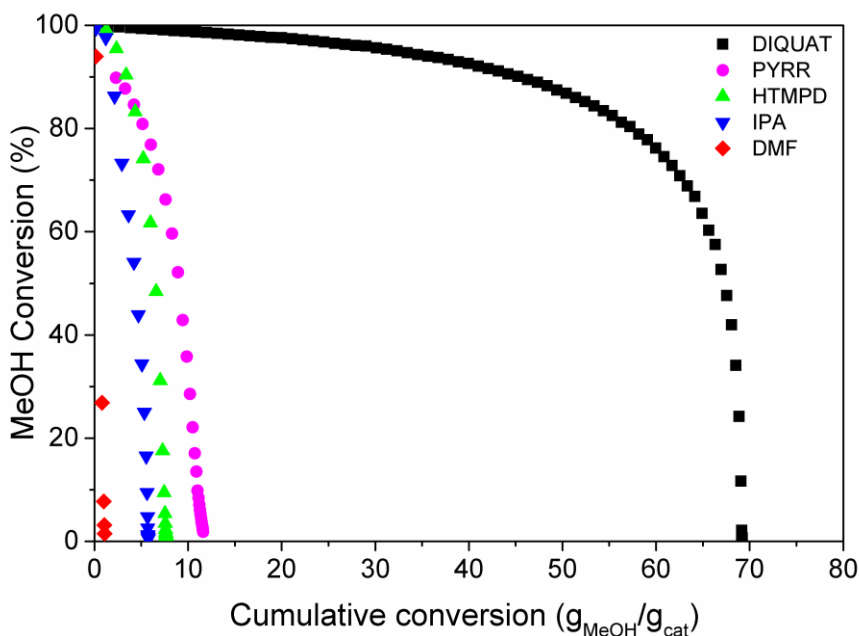

Figure 7 MeOH conversion plotted against cumulative conversion, WHSV = 2 h^{-1} and T = 400 °C

rationalize the influence of pore length on conversion capacity, the correlation between these two parameters is presented in Figure 8.
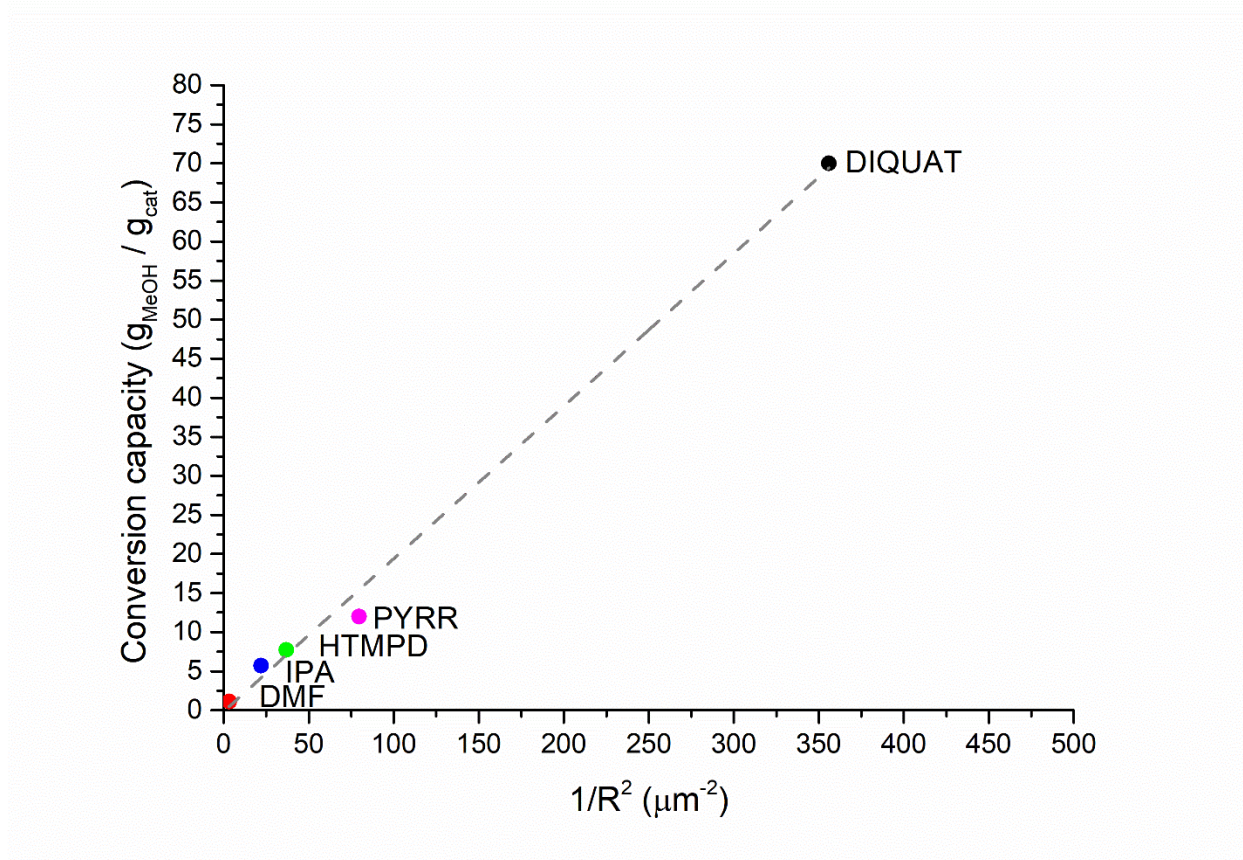
Figure 8 Methanol conversion capacity as a function of the reciprocal squared pore length (R)

The relationship between catalytic lifetime in MTH and crystal size has been recently investigated for ZSM-11 (MEL)[17], where a correlation with the characteristic diffusion time scales (D/R^2) was proposed, D being the diffusional coefficient and R the crystal size, suggesting an influence of diffusional effect caused by both the topology (D) and morphology (R).

For the MTT topology, the same quadratic correlation on diffusional path was found, using the conversion capacity instead, as shown in eq. 4.

$$Conversion\ capacity\left(\frac{g_{MeOH}}{g_{cat}}\right) = \frac{0.195}{R(\mu m)^2} \qquad (R^2 = 0.995) \qquad (eq.\ 4)$$

The product selectivities as a function of time on stream are shown in Figure 9. A direct comparison is hampered by the very different lifetimes of the catalysts, and in this comparison, less emphasis will be placed on the very rapidly deactivating DMF sample. By comparing the selectivities of the different catalysts in Table 5, it can be seen that the selectivities at full conversion for all catalyst are very similar. The amount of produced aromatics and ethene is very low (below 3% and 8% respectively), in line with the notion that under these reaction conditions, ethene is mostly produced by dealkylation from the arene cycle[42]. Propene can be derived from both cycles and the C_{4+} are mainly produced from the alkene cycle[43]. Therefore the C_3/C_2 ratio is higher for ZSM-23 compared to three dimensional 10-ring zeolites such as ZSM-5, where both cycles are active. Moreover, the selectivities follow the same trend during deactivation, suggesting that the reaction takes place under shape-selective conditions inside the pore system of the crystals. Noticeable is the decrease of all C_2-C_5 products with catalyst deactivation, while C_{6+} is increasing, probably caused by a lower cracking activity[7] due to the blockage of strong acid sites, suggesting the same deactivation mechanism for all the catalyst. When the highest selectivity for C_{6+} is reached, at around 20% conversion, the catalyst quickly deactivates and methane become the main product, which can be formed by direct reaction of methanol with methoxy groups[44], from methanol itself[45] or from the hydrocarbon pool species[46,47].
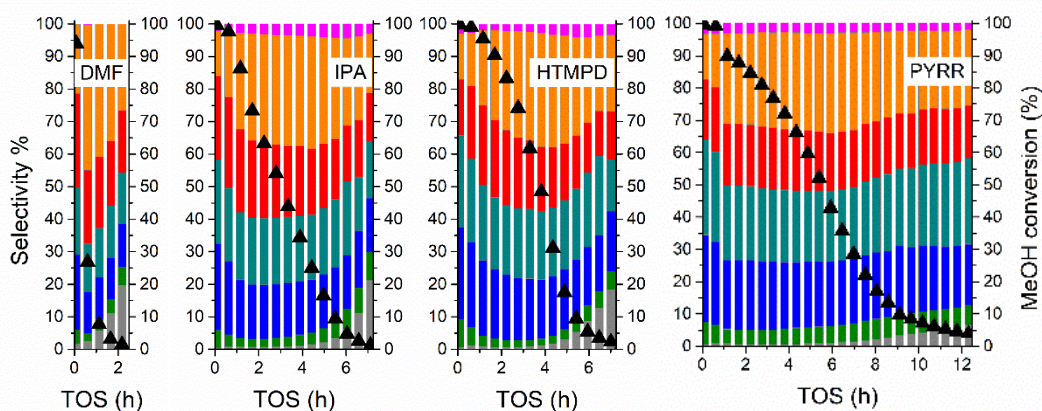
It may be noted that the increase in selectivity for the heaviest C_{6+} with TOS is more pronounced for the DIQUAT catalyst, having the smallest particle dimensions. This catalyst also displays a higher selectivity towards C_5 and thus lower towards C_3 and C_4 than the other catalysts at less than 100 % conversion. Another peculiar trait of the DIQUAT sample is the lower amount of aromatic products and ethane at lower conversion levels, while for the other samples a constant amount of

aromatics is produced after a steady state of 30 min is reached. Overall, the data suggest that the particle size plays a major role in catalyst deactivation, while the influence on product selectivity at near full conversion is rather small.

Table 5. Total conversion capacity, product selectivity in the MTH reaction at 400 °C, WHSV = 2 gg^{-1} over ZSM-23s compared with the average crystal length.

[a] After 5 min of TOS, [b]Excluding aromatic molecules,[c] Based on TEM measurement of weight-averaged length of the crystal along c

Sample	Conversion capacity (g_{MeOH} / g_{cat})	Initial conversion (C%)[a]	Selectivity at full conversion (5 min TOS)							Average crystal length (nm) [c]
			CH$_4$	C$_2$	C$_3$	C$_4$	C$_5$	C$_{6+}$[b]	C$_{Arom}$	
DIQUAT	70	99.8	0.4	7.9	27.9	24.9	21.3	14.9	2.7	50
PYRR	12	99.6	0.6	6.9	26.9	29.5	18.7	14.0	3.3	110
HTMPD	7.7	100	0.7	8.5	28.3	28.3	17.2	14.1	3.0	160
IPA	5.7	100	0.5	5.4	26.6	25.8	25.7	13.8	2.2	210
DMF	1.1	94.0	1.6	4.4	23.1	20.7	28.8	21.2	0.2	550
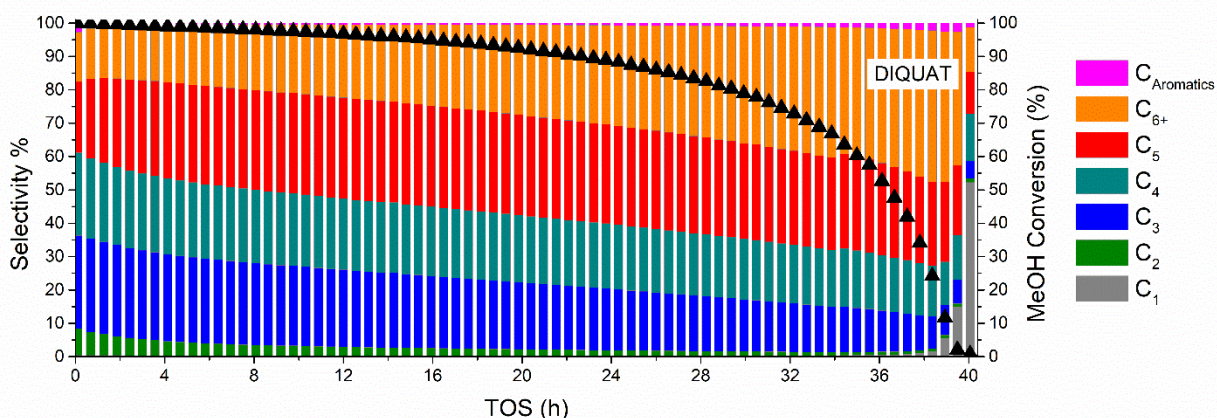
Figure 9. Product selectivity as a function of time on stream, WHSV = 2 h⁻1 and T = 400 °C.

4. Conclusions

A series of zeolite ZSM-23 catalysts with different crystal sizes has been prepared by using five different organic structure-directing agents. The crystallographic analysis from both XRD and electron diffraction reveal that the series of samples have different crystal lengths along the orientation parallel to the one-dimensional channels, ranging from 50 to above 500 nm. XRD analysis reveals that the preparation involving DMF as directing agent led to an intergrowth material. Infrared and NMR spectroscopies were used to identify the number, the nature (Lewis and Brønsted) and strength of acidic sites.

A change in crystal size from 50 to above 500 nm leads to an almost two order of magnitude higher methanol conversion capacity. A quadratic correlation between conversion and average crystal size is found. As the channels of the MTT structure are in the micropore size (0.5 nm), the removal of diffusion limitations and higher concentrations of pore openings[48] are both plausible explanations of the longer lifetime when the one-dimensional pore length is in the nanosized range, particularly in case of the DIQUAT sample. Our findings suggest that ZSM-23 is a valid alternative to other zeolites for processes targeted towards linear and branched hydrocarbons and when a low amount of aromatic products is desired.

Acknowledgments

References

1 U. V. Mentzel, S. Shunmugavel, S. L. Hruby, C. H. Christensen and M. S. Holm, *J. Am. Chem. Soc.*, 2009, **131**, 17009–17013.
2 N. Y. Chen and W. J. Reagan, *J. Catal.*, 1979, **59**, 123–129.
3 M. Westgård Erichsen, S. Svelle and U. Olsbye, *J. Catal.*, 2013, **298**, 94–101.
4 H. Koempel and W. Liebner, in *Studies in Surface Science and Catalysis*, eds. F. Bellot Noronha, M. Schmal and E. Falabella Sousa-Aguiar, Elsevier, 2007, vol. 167, pp. 261–267.
5 U. Olsbye, S. Svelle, M. Bjørgen, P. Beato, T. V. W. Janssens, F. Joensen, S. Bordiga and K. P. Lillerud, *Angew. Chem. Int. Ed.*, 2012, **51**, 5810–5831.
6 J. Topp-Jørgensen, in *Studies in Surface Science and Catalysis*, ed. C. D. C. D.M Bibby R. F. Howe and S. Yurchak D. M., Elsevier, 1988, vol. 36, pp. 293–305.
7 S. Teketel, S. Svelle, K.-P. Lillerud and U. Olsbye, *ChemCatChem*, 2009, **1**, 78–81.
8 S. Teketel, W. Skistad, S. Benard, U. Olsbye, K. P. Lillerud, P. Beato and S. Svelle, *ACS Catal.*, 2012, **2**, 26–37.
9 M. S. Holm, E. Taarning, K. Egeblad and C. H. Christensen, *Catal. Today*, 2011, **168**, 3–16.
10 A. A. Rownaghi and J. Hedlund, *Ind. Eng. Chem. Res.*, 2011, **50**, 11872–11878.
11 P. del Campo, P. Beato, F. Rey, M. T. Navarro, U. Olsbye, K. P. Lillerud and S. Svelle, *Catal. Today*, 2018, **299**, 120–134.
12 P. del Campo, U. Olsbye, K. P. Lillerud, S. Svelle and P. Beato, *Catal. Today*, 2018, **299**, 135–145.

13 J. Wang, S. Xu, J. Li, Y. Zhi, M. Zhang, Y. He, Y. Wei, X. Guo and Z. Liu, *RSC Adv.*, 2015, **5**, 88928–88935.

14 N. Nishiyama, M. Kawaguchi, Y. Hirota, D. Van Vu, Y. Egashira and K. Ueyama, *Appl. Catal. Gen.*, 2009, **362**, 193–199.

15 H.-G. Jang, H.-K. Min, J. K. Lee, S. B. Hong and G. Seo, *Appl. Catal. Gen.*, 2012, **437–438**, 120–130.

16 I. Pinilla-Herrero, C. Márquez-Álvarez and E. Sastre, *Catal. Today*, 2016, **277, Part 1**, 29–36.

17 Y. Shen, T. T. Le, D. Fu, J. E. Schmidt, M. Filez, B. M. Weckhuysen and J. D. Rimer, *ACS Catal.*, 2018, **8**, 11042–11053.

18 R. Khare, D. Millar and A. Bhan, *J. Catal.*, 2015, **321**, 23–31.

19 A. Molino, K. A. Łukaszuk, D. Rojo-Gama, K. P. Lillerud, U. Olsbye, S. Bordiga, S. Svelle and P. Beato, *Chem. Commun.*, 2017, **53**, 6816–6819.

20 A. C. Rohrman, R. B. LaPierre, J. L. Schlenker, J. D. Wood, E. W. Valyocsik, M. K. Rubin, J. B. Higgins and W. J. Rohrbaugh, *Zeolites*, 1985, **5**, 352–354.

21 H. J. Lee, S. H. Kim, J. H. Kim, S. J. Park and S. J. Cho, *Microporous Mesoporous Mater.*, 2014, **195**, 205–215.

22 S.-H. Lee, C.-H. Shin, D.-K. Yang, S.-D. Ahn, I.-S. Nam and S. B. Hong, *Microporous Mesoporous Mater.*, 2004, **68**, 97–104.

23 A. Moini, K. D. Schmitt, E. W. Valyocsik and R. F. Polomski, *Zeolites*, 1994, **14**, 504–511.

24 C.-H. Cheng and D. F. Shantz, *J. Phys. Chem. B*, 2005, **109**, 7266–7274.

25 S. Ernst, R. Kumar and J. Weitkamp, in *Zeolite Synthesis*, American Chemical Society, 1989, vol. 398, pp. 560–573.

26 B. Wang, Z. Tian, P. Li, L. Wang, Y. Xu, W. Qu, Y. He, H. Ma, Z. Xu and L. Lin, *Microporous Mesoporous Mater.*, 2010, **134**, 203–209.

27 Q. Wu, X. Wang, X. Meng, C. Yang, Y. Liu, Y. Jin, Q. Yang and F.-S. Xiao, *Microporous Mesoporous Mater.*, 2014, **186**, 106–112.

28 B. Marler, C. Deroche, H. Gies, C. A. Fyfe, H. Grondey, G. T. Kokotailo, Y. Feng, S. Ernst, J. Weitkamp and D. E. Cox, *J. Appl. Crystallogr.*, 1993, **26**, 636–644.

29 S. I. Zones, R. J. Darton, R. Morris and S.-J. Hwang, *J. Phys. Chem. B*, 2005, **109**, 652–661.

30 M. M. J. Treacy, J. M. Newsam and M. W. Deem, *Proc R Soc Lond A*, 1991, **433**, 499–520.

31 B. H. Toby and R. B. Von Dreele, *J. Appl. Crystallogr.*, 2013, **46**, 544–549.

32 A. Katerinopoulou, T. Balic-Zunic and L. F. Lundegaard, *J. Appl. Crystallogr.*, 2012, **45**, 22–27.

33 B.-T. L. Bleken, D. S. Wragg, B. Arstad, A. E. Gunnæs, J. Mouzon, S. Helveg, L. F. Lundegaard, P. Beato, S. Bordiga, U. Olsbye, S. Svelle and K. P. Lillerud, *Top. Catal.*, 2013, **56**, 558–566.

34 A. W. Burton, S. I. Zones, T. Rea and I. Y. Chan, *Microporous Mesoporous Mater.*, 2010, **132**, 54–59.

35 B. Wang, Z. Tian, P. Li, L. Wang, Y. Xu, W. Qu, H. Ma, Z. Xu and L. Lin, *Mater. Res. Bull.*, 2009, **44**, 2258–2261.

36 L. M. Parker and D. M. Bibby, *Zeolites*, 1983, **3**, 8–11.

37 J. M. Cowley, Ed., *Electron Diffraction Techniques: Volume 1*, Oxford University Press, Oxford, New York, 1992.

38 P. Wagner, O. Terasaki, S. Ritsch, J. G. Nery, S. I. Zones, M. E. Davis and K. Hiraga, *J. Phys. Chem. B*, 1999, **103**, 8245–8250.

39 J. Su, E. Kapaca, L. Liu, V. Georgieva, W. Wan, J. Sun, V. Valtchev, S. Hovmöller and X. Zou, *Microporous Mesoporous Mater.*, 2014, **189**, 115–125.

40 C. A. Fyfe, H. Grondey, Y. Feng, G. T. Kokotailo, S. Ernst and J. Weitkamp, *Zeolites*, 1992, **12**, 50–53.

41 Walter Loewenstein, *Am. Mineral.*, 1954, **39**, 92–96.

42 S. Svelle, F. Joensen, J. Nerlov, U. Olsbye, K.-P. Lillerud, S. Kolboe and M. Bjørgen, *J. Am. Chem. Soc.*, 2006, **128**, 14770–14771.

43 M. Westgård Erichsen, K. De Wispelaere, K. Hemelsoet, S. L. C. Moors, T. Deconinck, M. Waroquier, S. Svelle, V. Van Speybroeck and U. Olsbye, *J. Catal.*, 2015, **328**, 186–196.

44 Z. Wei, Y.-Y. Chen, J. Li, P. Wang, B. Jing, Y. He, M. Dong, H. Jiao, Z. Qin, J. Wang and W. Fan, *Catal. Sci. Technol.*, 2016, **6**, 5526–5533.

45 L. Kubelková, J. Nováková and K. Nedomová, *J. Catal.*, 1990, **124**, 441–450.

46 H. Schulz, *Catal. Today*, 2010, **154**, 183–194.

47 H. Schulz and M. Wei, *Top. Catal.*, 2014, **57**, 683–692.

48 F.-F. Wei, Z.-M. Cui, X.-J. Meng, C.-Y. Cao, F.-S. Xiao and W.-G. Song, *ACS Catal.*, 2014, **4**, 529–534.